NUMERICAL STUDY OF HEAT DIFFUSION CONTROLLED BUBBLE GROWTH IN A PRESSURIZED LIQUID

G. Giustini, J. Murallidharan
Imperial College London
g.giustini12@imperial.ac.uk; j.murallidharan@imperial.ac.uk;

Y. Sato, B. Niceno
Paul Scherrer Institute
yohei.sato@psi.ch; bojan.niceno@psi.ch

V. Badalassi, S. Walker
Imperial College London
v.badalassi@imperial.ac.uk; s.p.walker@imperial.ac.uk

ABSTRACT

For water-cooled nuclear reactors an ability to predict various aspects of boiling is important for both safety and design. Practical component-scale modelling is necessarily done by semi- mechanistic, semi-empirical approaches, generally based on heat flux partitioning. This needs to be informed by multiple detailed experimental observations of boiling behavior. Such measurements are difficult to make, especially at conditions of relevance to nuclear reactors, and now much effort is being applied to microscopic computational modelling of the detailed boiling process. Such analyses are difficult, with interface motion, heat transfer, phase change and mass transfer, alongside 'normal' fluid mechanics. They are also hard to validate. In this paper we attempt to predict one of the few cases for which there is an analytical solution of a reasonably representative model; the case of an isolated bubble growing in superheated fluid. We employ the interface-tracking code PSI-Boil (Y. Sato, B. Niceno, *Journal of Computational Physics, Volume 249, 15 September 2013, Pages 127-161)*. Good results are obtained, but the work did highlight issues in studies of these microscopic phenomena, when the vapour flows associated with the mass transfers become the dominant flow. Spurious currents are generated associated with imperfect modelling of the high-curvature geometries. Eliminating these imposes particularly stringent requirements on aspects of the modelling. This problem is identified, and methods to eliminate the spurious currents under the relatively simple conditions of the present study are developed. These methods in turn provide pointers to a treatment in more general cases.

KEYWORDS
Bubble growth, boiling heat transfer, high pressure, Interface Tracking, CFD.

1. INTRODUCTION

For water-cooled nuclear reactors one of the major challenges to greater use of computational fluid dynamics for understanding and predicting their thermal hydraulic and safety performance is the ability of such tools to deal reliably with issues associated with a phase change [1]. These issues include boiling, void distribution, heat transfer performance, and so on.

The gross range of length scales associated with such a prediction is a major contributor to its difficulty. The component-scale to which models must be applied is of order meters (example a fuel assembly). However, the length scale associated with the fundamental processes at work extends down to microns,

for bubble nucleation and initial growth, up to millimetres for bubble departure and advection into the flow.
This component-scale modelling is generally tackled via "normal" Eulerian-Eulerian two phase CFD models, augmented with particular closure relations at the wall that attempt semi-mechanistically to incorporate boiling effects [2]. Such incorporation normally involves an approach broadly classed as "heat flux partitioning", where the postulated heat transfer mechanisms associated with boiling are represented in a semi-empirical, semi-mechanistic fashion. This semi-empirical, semi-mechanistic representation is largely based upon experimental observations, but these are understandably fairly sparse, particularly at conditions relevant to operating reactors.
Modern interface-tracking computational fluid dynamics in principle allows highly detailed predictions to be made of the processes associated with bubble growth and departure, covering both the hydrodynamic and the thermal phenomena. In a nuclear context, the need to provide insights and data to improve component-scale representations has provided motivation for intense study in recent years of the fundamental processes of boiling, and the associated attempts to represent these by "exact" mechanistic CFD models.
This present work is in this spirit. Whilst in principle such treatments might be exact, they are of course highly challenging, involving interface tracking, phase change, and heat transfer, along with surface-contact effects. As part of the activity of developing, improving and validating computational models for this purpose, we here study a simpler subset of the full problem. We investigate the growth of an isolated bubble in a uniform body of superheated stationary fluid. As will be seen, this is a useful and challenging exercise in its own right, but it is also directly relevant to the case of the growth of vapour bubbles in very high-pressure conditions. Here surface tension effects limit the contact of bubbles with the heated surface [3], possibly favouring the generation of vapour from surrounding superheated "bulk" liquid, rather than the “micro-layers" believed to be important at low pressures.

In this contribution, we present a CFD analysis of bubble growth at high (up to 45 bar) pressure in the absence of gravity. We use Direct Numerical Simulation coupled with an interface tracking method to simulate the growth of a spherical vapor bubble expanding in a stationary, superheated pool of water. We predict the bubble growth rate as a consequence of the initial temperature distribution. A short review of the relevant published works is given in section 2. In section 3 the details of our computational model are explained, and a discussion of the results of our simulations is presented in section 4. Conclusions are drawn in section 5.

2. LITERATURE REVIEW

2.1. Analytical studies on bubble growth

The first physical models of bubble growth in a body of liquid are due to Plesset et al. [4, 5] and Forster et al. [6, 7]. Bubble expansion in a pool of superheated liquid in the absence of gravity was modeled under the assumption that the bubble is spherical in shape and that the vapor inside it has uniform temperature and pressure, equal respectively to the liquid temperature at the vapor-liquid interface and to the equilibrium vapor pressure at such temperature.

2.1.1. Inertia and heat diffusion controlled bubble growth regimes

Just after nucleation, the bubble radius can be small enough for the Laplace pressure (the externally-imposed system pressure, plus the pressure associated with the surface tension) to increase the liquid surface temperature required for phase stability [8], [9]. This condition is only metastable, and if the system is perturbed, the bubble can grow or collapse. If perturbing the system results in growth, during its expansion the interface temperature reduces, and eventually, at a large radius, reaches the saturation value at the system pressure when the Laplace pressure is small compared to the system pressure.
This initial growth stage is not fully understood yet, but it is believed that inertia plays a role[5] [10]. Once inertial forces cease to be significant, the bubble growth rate is essentially determined by the rate of

transport of heat to the gas-liquid interface. This generates vapour that causes the bubble to grow, and quasi-static quantitative modelling to predict growth rate is possible.
Assuming that inertia and viscous forces are negligible, Scriven [11] modelled bubble growth as a transient heat conduction problem in a spherical system with a moving boundary (the liquid-vapor interface). The vapor is assumed of constant and uniform temperature. In particular, the dependence of the saturation temperature on pressure changes associated with changes in bubble size, and hence Laplace pressure, are neglected. The heat conduction problem is solved in the liquid. The production of vapor is taken as being proportional to the heat flux at the bubble wall, with this wall taken to be at the saturation temperature. The vapour production rate is thus limited by the rate of transfer of heat across the thermal boundary layer that is formed in the liquid due to the presence of the bubble. In this heat diffusion-controlled regime, it turns out that the bubble growth rate reduces at a rate proportional to the square root of time, and the constant of proportionality can be evaluated semi-analytically. Mikic et al. [12] quantified diffusion-controlled bubble growth on the basis of a Jakob number; essentially the product of the ratio of sensible to latent heat, multiplied by the expansion rate. Non-dimensional growth curves were developed, and within the limit of diffusion-controlled growth, the non-dimensional bubble radius was found to depend on the square root of the non-dimensional time:

$$R^{+} = t^{+1/2} \tag{1}$$

A model based on heat conduction through a near-wall superheated liquid layer was introduced by Han et al. [13] to quantify the growth rates of bubbles growing at a heated wall, in the presence of gravity. A similar approach was applied to micro gravity conditions by Lee et al. [14].

2.2. Experimental investigations

The complexity of the nucleate boiling process constitutes an obstacle to the quantification of bubble growth rates given an initial temperature distribution in the fluid. Only limited control of the temperature near the heater is achievable, due to the randomness of the mechanism of growth and detachment of bubbles. The main cause for this is bubble detachment and rise, and the associated turbulence, which are promoted by buoyancy forces. Reduction of the gravitational acceleration allows increased control of the temperature distribution near the heater.

2.2.1. Growth of bubbles in zero gravity

Boiling experiments in reduced gravity have been reported by numerous authors over several decades [15-22]. Pool boiling curves and CHF data were collected at several gravity levels for various operating fluids. As regards single bubble growth, a comparison between theory and experiment was conducted by Lee et al. [14], who performed boiling experiments with R-113 on a gold heater at a high (~ 50) Jakob number in microgravity. In their work, it was found that the experimental results can be predicted with a transient conduction model [10]. The model can predict the bubble growth rate given an initial temperature distribution in the liquid. Two limiting cases exist for the initial temperature distribution, namely that of uniform superheat within the body of liquid, whose temperature is thus equal to the wall temperature, and that of a thermal boundary layer completely enclosing the bubble surface. The authors found that the experimental results were reproduced choosing an appropriate weighted average of the two cases. The weights were obtained *a posteriori* using the experimental growth rate.

2.3. CFD modelling of bubble growth

Simulation of bubble growth using Computational Fluid Dynamics requires more “modeling” than does single phase DNS. A means for incorporating the force associated with the gas-liquid interface is necessary, as is a model for evaluation of the interphase mass flux. Surface tension effects are modeled via a term in the momentum balance equation that vanishes anywhere except at the interface itself. The most common implementation treats this term as a body force [23] active in a few cells (typically three) around the interface. The motion of the gas-liquid interface can be captured with interface tracking techniques, which involve the solution of an additional advection equation for a scalar quantity used to

locate the interface, which is assumed to have zero mass and thickness [24]. As regards accounting for the production of vapour at the gas-liquid interface, at moderate ($\sim 1\ kg/m^2s$) interphase mass fluxes, and in systems that are large in terms of thermal capillary lengths [25], it is appropriate to use the so called "Stefan condition" [26]. With this model, the interphase mass flux is evaluated as proportional to the jump in heat flux across the interface. Welch et al. [27] coupled this approach with the mass-conservative Volume Of Fluid interface tracking method, while Gibou et al. [28] did with the Level Set method and Sato et al. [29] used a mass-conserving Constrained Interpolation Profile (CIP-CISL2) technique.

In this work, bubble growth is studied assuming that gas and liquid are incompressible Newtonian fluids with constant mechanical and thermophysical properties, here evaluated at the saturation temperature at the system ambient pressure. It is assumed that the vapour is at the equilibrium saturation temperature corresponding to the externally imposed system ambient pressure: the effect of the Laplace pressure on the equilibrium saturation temperature of the vapour is neglected here. Also the interface temperature is assumed equal to the saturation value at the system ambient pressure, and the curvature correction of the interface temperature is neglected. In the conditions of interest, these effects are relevant only for bubble radii at least two orders of magnitude smaller than those considered in this work. Based on the assumptions summarised above, application of the Stefan condition to the present problem reduces to calculating the rate of production of vapour occurring at the interface as proportional to the heat flux on the liquid side of the interface. A consequence of this approach is that, if the numerical computation is correct, throughout the whole time of the computation the bubble conserves its spherical shape and the vapour remains at the saturation temperature

3. COMPUTATIONAL MODEL

3.1. The numerical method

3.1.1. Navier-Stokes solver coupled with the CIP-CISL2 Interface Tracking method

Use is made of a Finite Volume Navier-Stokes solver employing a staggered arrangement on a Cartesian grid [30]. The pressure-velocity coupling is obtained with a projection method [30]. The Constrained Interpolation Profile (CIP-CISL2) method [31] is used to track the motion of the gas-liquid interface. With this method, an advection equation is solved for the liquid volume fraction ϕ, termed a 'colour function', whose 0.5 contour is identified as the gas-liquid interface. To avoid the smearing of ϕ, a sharpening equation [32] is employed. The coupling of CIP-CSL2 and the sharpening equation is given in [31]. The details of the evaluation of temperature gradient in the liquid near the interface, performed with a strategy similar in spirit to that employed by Gibou et al. [28], are reported in [29]. The solution procedure starts with computing the vapor production per unit volume at the interface at the current time step based on the color function and temperature distribution at the previous time step:

$$\dot{m} = \frac{\mathbf{q}_l \cdot \mathbf{n} - \mathbf{q}_g \cdot \mathbf{n}}{h_{fg}} \cdot \frac{S_{int}}{V_{cell}} \tag{2}.$$

Then the velocity and pressure fields are updated by the projection method:

$$\begin{aligned} \nabla \cdot \mathbf{u} &= \left(\frac{1}{\rho_g} - \frac{1}{\rho_l} \right) \dot{m} \\ \rho \frac{\partial \mathbf{u}}{\partial t} + \rho \left(\nabla \cdot \left(\mathbf{u}\mathbf{u} \right) - \mathbf{u} \left(\nabla \cdot \mathbf{u} \right) \right) &= -\nabla p + \nabla \cdot \left(\mu \left(\nabla \mathbf{u} + \left(\nabla \mathbf{u} \right)^T \right) \right) + \rho \mathbf{g} + \sigma \kappa \nabla \phi \end{aligned} \tag{3},$$

where a generic property a (density, viscosity or thermal conductivity) is expressed as $a = a_l + (1 - \phi) a_g$ and surface tension (the last term on the RHS on equation (3)) is treated as a body force as in [23]. The next step is updating the color function:

$$\frac{\partial \phi}{\partial t} + \nabla \cdot \left(\phi \mathbf{u} \right) = -\frac{\dot{m}}{\rho_l} \tag{4}.$$

Given the resulting color function distribution field, the temperature distribution is determined solving the energy equation:

$$C_p \left(\frac{\partial T}{\partial t} + \nabla \cdot T\mathbf{u} - T \nabla \cdot \mathbf{u} \right) = \nabla \cdot \left(k \nabla T \right) \tag{5}.$$

With the interface temperature taken as the saturation temperature at the system ambient pressure, as noted above, updating of the temperature field ends the solution procedure for that step. More details about the numerical procedures involved are available in [29].

3.1.2. Curvature calculation

Curvature of the liquid-vapor interface is calculated from:

$$\kappa = -\left(\nabla \cdot \mathbf{n} \right), \tag{5}$$

where $\mathbf{n}$ is the unit normal vector to the liquid-vapor interface. For the present case of very small cavities with high curvature, the approximations associated with evaluating this in a discrete form contribute to causing spurious circulatory currents to be generated in the adjacent fluids. This is referred to in the following as *original curvature calculation*. However, for this particular study of spherical voids, we are able to use a particular, and very accurate, curvature value of 2/*R* (referred to in the following as *improved curvature calculation*), and this contributes greatly to their reduction [33]. We will return to this point.

4. SIMULATION OF A SCRIVEN BUBBLE

4.1. Test cases

The simulation setup and material properties for the Scriven bubble test cases are shown in Figure 1 and Table 1.

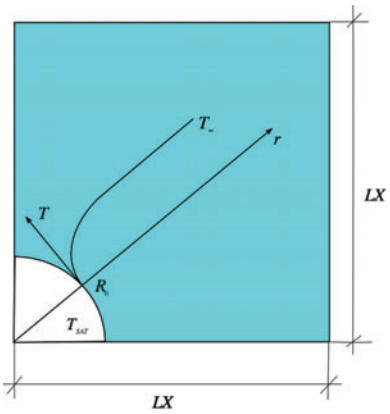

Figure 1. Simulation setup for the Scriven bubble test cases.

Property	Water at 22.7 bar		Water at 45 bar	
	Liquid	Gas	Liquid	Gas
$\rho\ [kg/m^3]$	830.0	13.5	787.6	22.7
$\mu\ [Pa \cdot s]$	117.3×10^{-6}	16.6×10^{-6}	103.0×10^{-6}	17.7×10^{-6}
$k\ [W/(m \cdot K)]$	641.0×10^{-3}	45.2×10^{-3}	608.0×10^{-3}	53.7×10^{-3}
$c_p [J/(kg \cdot K)]$	4667.6	3486.3	4940.0	4230.0
$\sigma [N/m]$	31.2×10^{-3}		24.5×10^{-6}	
$h_{fg} [J/kg]$	1821.5×10^{3}		1675.9×10^{3}	
$T_{sat}\ [K]$	500.7		530.0	

Table 1. The properties of water at 22.7 and 45

The conditions simulated are chosen to be broadly similar to published nucleate boiling experiments at high pressure conducted in normal (Earth) gravity [34]. The spherical symmetry of the problem is exploited to simulate a sector corresponding to only 1/8 of the physical domain; one quarter of the 'top half' of a bubble. The computational domain is a cube of side *LX*, with symmetric boundary conditions at the boundaries crossed by the gas-liquid interface and outlet conditions elsewhere. The normal pressure and temperature gradients are set to zero at the outlet boundaries. The domain size has to be chosen to

accommodate the bubble and minimise the disturbance due to the outlet condition, albeit constrained by computational cost. Geometrical and physical parameters for the two cases of interest are reported in Table 2. Initial conditions need to be specified. Inside the bubble, the vapor is set to the saturation temperature T_{sat}.

Table 2. Scriven bubble simulation setup

Parameter	22.7 bar case	45 bar case
LX $[\mu m]$	238.0	78.36
R0 $[\mu m]$	79.4	30.05
Δt_0 $[ms]$	5	1.295
ΔT $[K]$	6.13	6.13
Ja	0.966	0.627

Specification of the initial temperature field in the liquid is more complex. The remote liquid is initially taken to be superheated by an amount $\Delta T = T_\infty - T_{sat}$. The computational model cannot start from a zero bubble radius. Whilst one would expect the influence of an arbitrary choice of initial conditions to decline rapidly, if the initial bubble size specified were small enough, it is sensible to use what we believe is a plausible set of initial conditions. This is done by taking one of the results due to Scriven, from which we can estimate the initial radius believed to obtain after some corresponding early time:

$$R_0 = 2\beta\sqrt{\alpha_l \Delta t_0} \tag{6}$$

The density ratio in the present case is high enough to allow use of the following asymptotic expansions for the growth constant β [11]:

$$\varphi = \frac{\rho_l c_{pl} \Delta T}{\rho_g \left(h_{fg} + \left(c_{pl} - c_{pg}\right)\Delta T\right)}$$
$$\beta = \frac{\varphi}{\sqrt{\pi/3}} + 4/9 \tag{7}.$$

The initial temperature distribution is evaluated based on the analytical solution obtained in the original work by Scriven. The formula for evaluating the temperature profile in the liquid as a function of distance from the interface - $T(R - R_0, \Delta t_0)$ - is[29]:

$$T = T_\infty - 2\beta^2 \left(\frac{\rho_g \left(h_{fg} + \left(c_{pl} - c_{pg}\right)\Delta T\right)}{\rho_l c_{pl}} \right) \int_{1-R(t)/r}^{1} exp\left(-\beta^2 \left(\left(1-\xi\right)^{-2} - 2\left(1 - \frac{\rho_g}{\rho_l}\right)\xi - 1 \right) \right) d\xi \tag{8},$$

where ξ represents a dummy variable. This is specified as the initial temperature distribution.

4.1.1. Numerical issues

We have mentioned spurious currents above, in the context of poorly calculated interface normals. The currents are caused because these normals appear in the surface tension term of the momentum balance equation. When there is little fluid motion (as in bubble growth at high pressure, which is rather slow compared to low pressure), the currents can pollute significantly the solution (particularly, in our case, the temperature distribution). Several approaches have been proposed to alleviate this problem. In this

particular case, since the only fluid motion expected is radially outwards, with the original curvature calculation, we impose a high value of the viscosity (ten times the viscosity of the liquid phase) in both the gas and liquid to limit spurious currents. The value of the artificial viscosity was chosen based on numerical experiments: keeping a constant discretization, four cases with increasing viscosities were run, and the total kinetic energy in the computational domain was monitored. It was expected a divergent behavior of the kinetic energy for the real viscosity case, due to the unphysical buildup of a recirculation flow pattern caused by the spurious currents. On the other hand, the simulations with the artificial viscosities were not expected to show this behavior. This trend actually emerges from Figure 2. The quantity plotted on the ordinate is obtained evaluating half of the square of one component of the velocity vector (thanks to the spherical symmetry of the problem, it has no importance which component, namely, in this case, along the x-direction) and summing over all the computational cells. Thus the quantity obtained can be interpreted as a specific kinetic energy, with units $\left[J \,/\, kg = m^2 \,/\, s^2\right]$. The monitored quantity increases for two reasons: i) the initial buildup of the spurious recirculation and ii) after the recirculating pattern is established, the region of the domain affected by it – localized near the interface – increases in size due to bubble expansion. Following the numerical experiment described, a value of the viscosity equal to ten times the liquid viscosity is adopted for both phases.

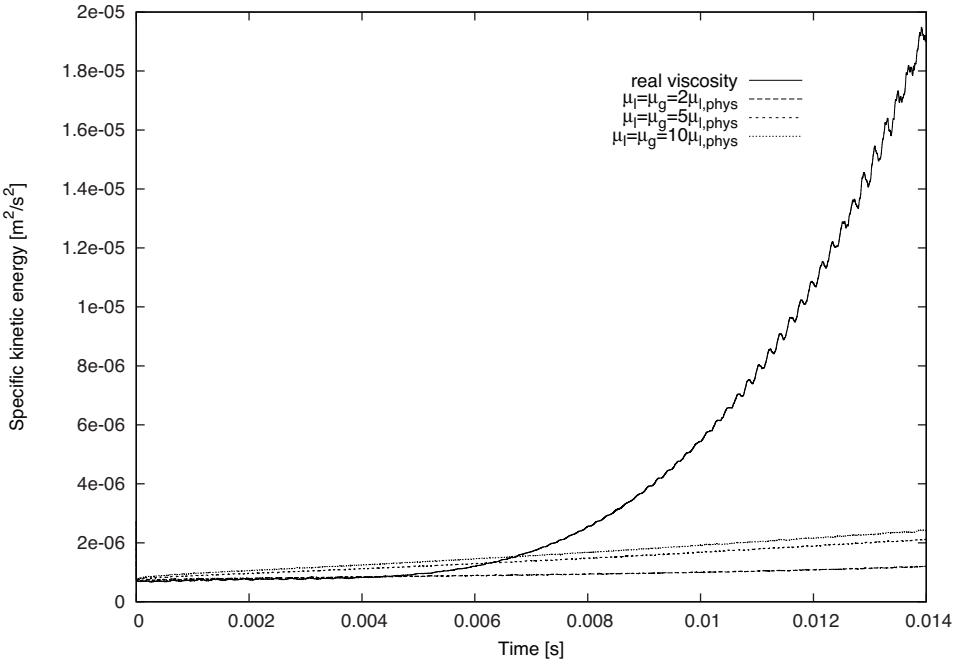

Figure 2. Temporal evolution of the kinetic energy in the domain for various viscosities.

On the other hand, with the improved curvature calculation, use of the physical viscosity is made. However, in order to apply the present methodology to a broader range of problems, it will be necessary to adopt a different calculation of the interface curvature. In the following, we present results for three cases: i) original curvature calculation with real viscosity, ii) original curvature calculation with artificial viscosity, iii) modified curvature calculation with real viscosity.

4.1.2. Results: 22.7 bar case

Results from a mesh independence study for the 22.7 bar case with the artificial viscosity are shown on the left hand side of Figure 3, where the analytical and numerically computed growth curves are plotted. Since the production of vapour is calculated based on the heat flux jump at the interface, the refinement is dictated by the need of resolving the thermal boundary layer in the water. In addition, a finer

discretization can in principle help in limiting the spurious currents. Three cases of equal-spacing grid with different resolution – 48, 72 and 144 cells per side – have been tested. Convergence towards the analytical solution is observed if the artificial viscosity is used. On the other hand, with the physical viscosity, the computed bubble radius differs significantly from the analytical solution, as seen in the right hand side of Figure 3.

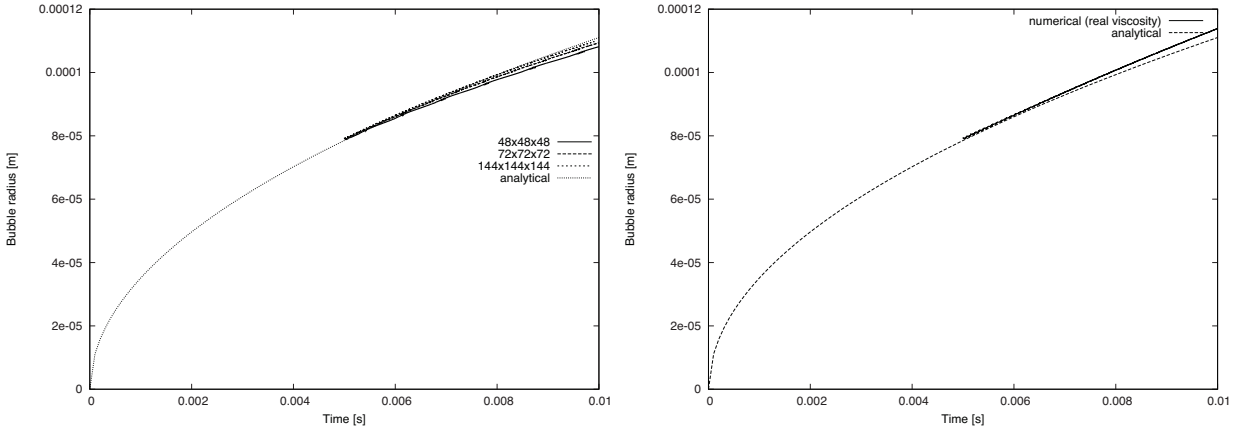

Figure 3. Left: mesh independence study for the 22.7 bar case with artificial viscosity. Right: growth rate obtained with the finest mesh with the real viscosity.

The difference in computed temperature and volumetric vapor production (kg/m^3s) fields after 8 ms between the real (fine mesh) and artificial (intermediate mesh) viscosity cases is shown in Figure 4. The spurious currents cause recirculating flow patterns near the gas-liquid interface that distort the temperature distribution in the liquid water. Since the production of vapor is calculated based on the temperature gradients in the water at the interface, non-uniform vapour production is predicted. It is seen that as a consequence of the increased viscosity, the intensity of the spurious currents is reduced and the large recirculation that appears near the bubble poles and equator if the real viscosity is used is damped. As a consequence, physically plausible temperature and volumetric vapor production distributions are obtained. On the other hand, the artificial viscosity does not seem to help limiting the absolute value of the spurious currents that does not seem to be reduced with respect to the physical viscosity case. In fact, some localized maxima of the velocity vector – pointing approximately in the normal direction to the interface - are localized at a few locations around the interface. The origin of these vectors is purely numerical, since they point in the direction opposite to bubble expansion.

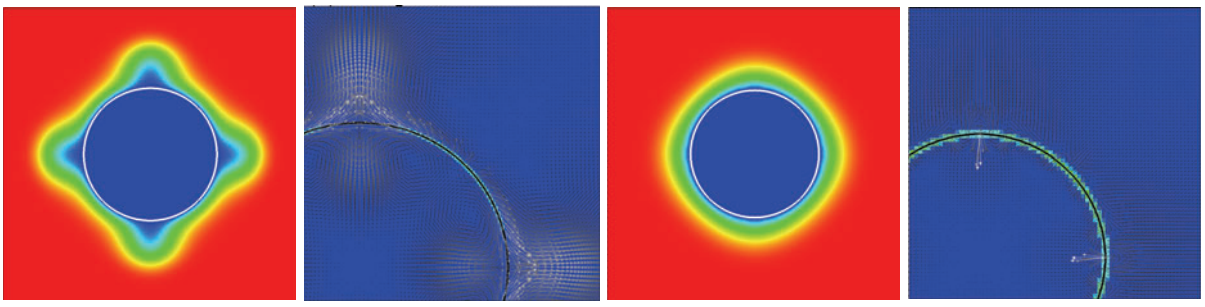

Figure 4. Scriven bubble, 22.7 bar. Temperature (left) and volumetric vapor production (center left) distributions after 8 ms using the real viscosity; the temperature varies from 500.7 K (blue) to 506.83 K (red), the maximum $\dot{m}$ is 86400 kg/m^3s, the maximum velocity vector intensity is 0.072 m/s. Temperature (center right) and volumetric vapor production (right) distributions after 8 ms using the artificial viscosity; the maximum $\dot{m}$ is 32100 kg/m^3s, the maximum velocity vector intensity is 0.039 m/s.

Growth rates obtained with an improved calculation of the interface curvature are shown in Figure 5. Convergence towards the analytical solution is observed if the mesh is refined and better agreement with the analytical growth rate is observed with respect to both the real viscosity and artificial viscosity cases with the original curvature calculation. The temperature and volumetric vapor production predictions are also improved. The thermal boundary layer remains spherical, as a consequence of the disappearance of the recirculating areas near the bubble poles and equator. In addition, the abnormally high velocity vectors appearing at some locations along the interface if the fictitious viscosity is prescribed are no longer present.

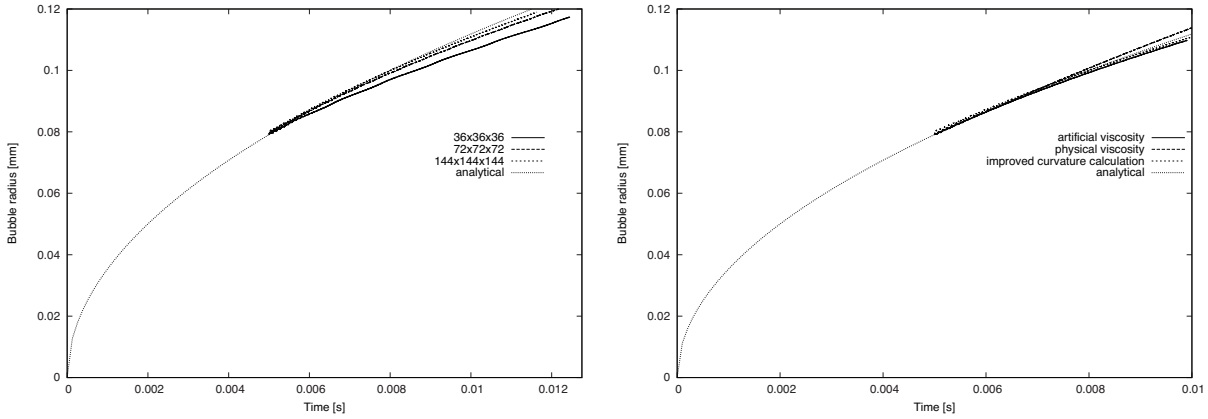

Figure 5. Left: mesh independence study for the 22.7 bar case using the improved curvature calculation and physical viscosity. Right: comparison between growth rates obtained with the finest mesh using artificial viscosity (original curvature computation), physical viscosity (original curvature computation) and the improved curvature computation.

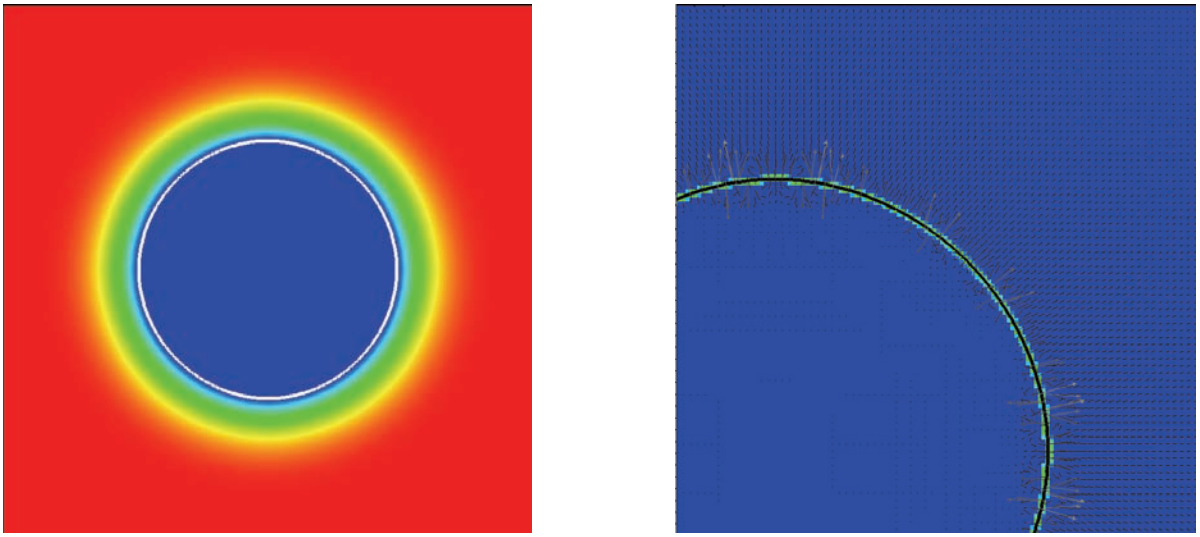

Figure 6. Temperature (left) and volumetric vapor production (right) distributions obtain for the 22.7 bar case after 11.75 ms using the real viscosity and improved curvature calculation; the maximum $\dot{m}$ is 53000 kg/m^3s, the maximum velocity vector intensity is 0.047 m/s.

4.1.3. 45 bar case: results

The methodology described for the 27 bar case is also applied to the 45 bar case. The conditions of the simulation at 45 bar result in a thicker – compared to the bubble radius - thermal boundary layer than the

22.7 bar case. Since the need to resolve this boundary layer is the main constraint on mesh size, no further refinement is required with respect to the 22.7 bar case (despite the smaller initial bubble radius), and the same discretisations as the previous case are used. The simulation begins at an earlier stage of bubble growth than did the 22.7 bar case considered in this study. As a consequence, the thermal boundary layer is thinner and having the same superheat the interphase mass transfer is more vigorous. In these conditions, the spurious currents have a smaller effect, and the temperature and volumetric production of vapor distributions are less distorted. A comparison between the analytical and numerical bubble growth curves obtained with the improved curvature calculation is shown on the left hand side of Figure 7. The growth rate obtained numerically with artificial viscosity agrees reasonably with the analytical solution. Interestingly, no significant difference in terms of growth rate is observed between the results obtained with the original curvature computation (using both artificial and physical viscosities) and the improved curvature computation, as is shown on the right hand side of Figure 7.

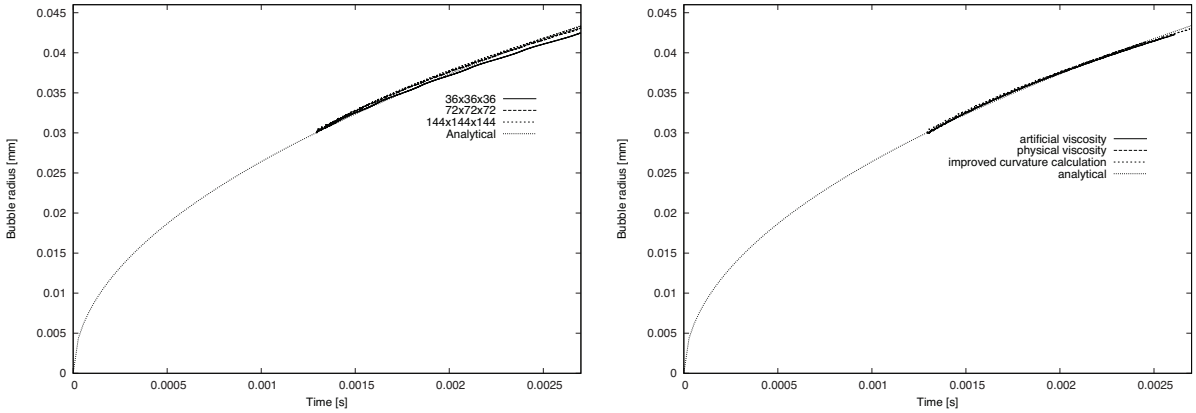

Figure 7. Left: mesh independence study for the 45 bar case using the improved curvature calculation and physical viscosity. Right: comparison between growth rates obtained with the finest mesh using artificial viscosity (original curvature computation), physical viscosity (original curvature computation) and the improved curvature computation.

However, significant differences appear in terms of temperature and volumetric production of vapor distributions, as shown in Figure 8.

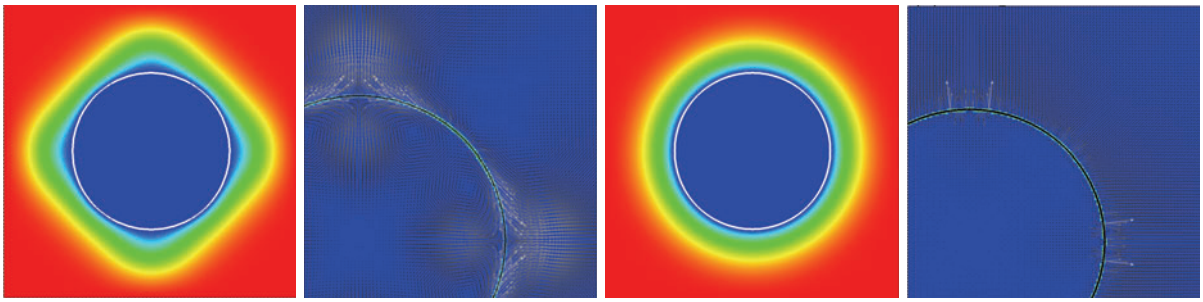

Figure 8. Scriven bubble, 45 bar. Temperature (left) and volumetric vapor production (center left) distributions after 2.5 ms using the real viscosity; the temperature varies from 530.0 K (blue) to 536.13 K (red), the maximum $\dot{m}$ is 504000 kg/m^3s, the maximum velocity vector intensity is 0.06 m/s. Temperature (center righ) and volumetric vapor production (right) distributions after 2.5 ms using the artificial viscosity; the maximum $\dot{m}$ is 439000 kg/m^3s, the maximum velocity vector intensity is 0.029 m/s.

As in the previous case, the increased viscosity has eliminated the two recirculating patterns at the polar and equatorial regions of the interface, and the velocity distribution results are improved. We notice however a small number of localized peaks of the velocity perturbation that have not been eliminated by increasing the viscosity.

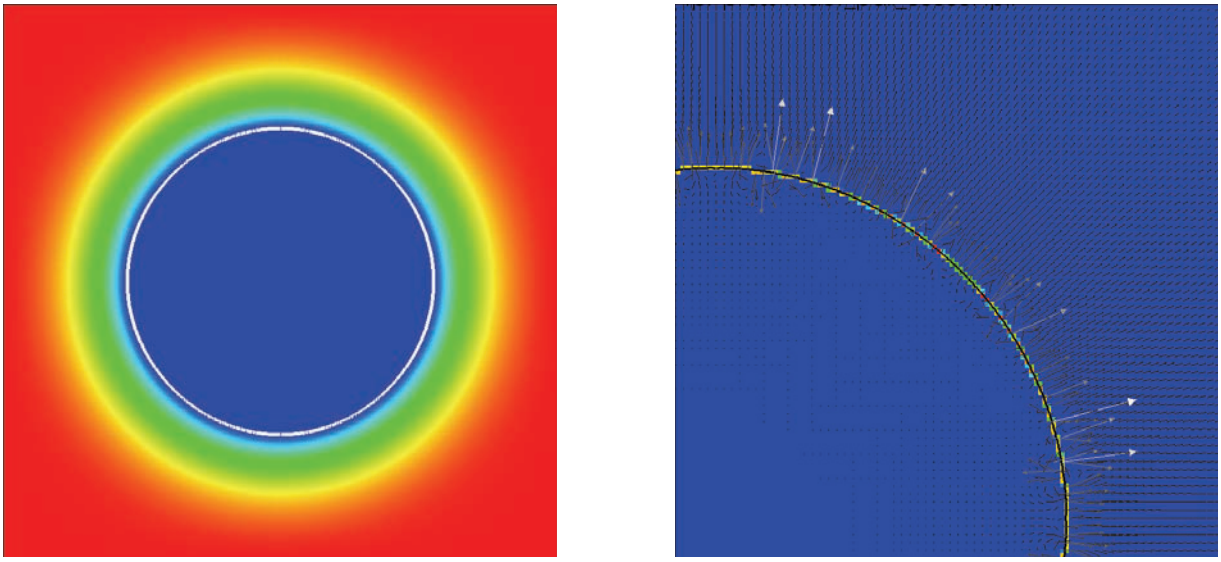

Figure 9. Temperature (left) and volumetric vapor production (right) distributions obtained for the 45 bar case after 2.5 ms using the real viscosity and improved curvature calculation; the maximum $\dot{m}$ is 400000 kg/m^3s, the maximum velocity vector intensity is 0.04 m/s.

The benefit of the improved curvature calculation is evident from Figure 9, where the temperature and volumetric production of vapor distributions after 2.5 ms are shown. Although localized peaks of the velocity vectors are still present, and some perturbations of the velocity field still affect a narrow region enclosing the interface, the recirculating patterns are no longer present, and overall the flow is radially outwards, as expected. No significant distortion of the thermal boundary layer is observed; as a consequence, the interphase mass transfer rate is evenly distributed along the interface. It is worth noting that the combined use of both of the methods devised to limit spurious currents was not sufficient to eliminate all perturbation of the velocity field near the interface. An abnormally high magnitude of the velocity vector – which is however directed radially, as expected - is observed near the poles and equator of the bubble. These perturbations are oscillatory. The spurious velocity vectors have been observed to point both inwards (as in Figure 4) and outwards. This occurrence does not have a measurable influence on the computed temperature and interphase mass transfer distributions, however the issue needs to be addressed in the future.

5. CONCLUSIONS AND FUTURE WORK

The results presented show that the interface tracking approach with phase change is able to produce predictions that are in very good agreement with the analytical solution for this problem. As such, they provide encouragement for the development of the approach for its application, in particular, to support the component-scale modelling of two phase flows in a nuclear context. However, there are various aspects where further research is plainly required. There are some simplifications in the approach taken associated with the use of conditions at the vapour-liquid interface that did not fully take into account the pressures associated with the high curvatures of bubbles in their early stages. Some work here may be valuable, albeit the importance of this will be first need to be assessed via a consideration of the actual

physical conditions likely to be of practical interest. Probably the greater issue is associated with the spurious currents generated in the solution. That these are indeed spurious, and that without them very accurate solutions can be obtained, was clearly demonstrated. However, whilst the approaches adopted to remove their effect, of non-physical use of a high viscosity, and the use of surface normals computed based on our a priori knowledge of the surface geometry, were very effective, these approaches are unlikely to be acceptable under the more general circumstances of real interest. Perhaps the major conclusion from this study is that the cause of, and remedy for the spurious currents needs to be more fundamentally identified and more generally based, in order for these methods to be used with confidence for the purposes discussed.

NOMENCLATURE

Roman:

A nondimensionalisation constant, equal to $\left(\frac{2\Delta T h_{fg}\rho_g}{3T_{sat}\rho_l}\right)^{1/2}$

B nondimensionalisation constant, equal to $\left(\frac{12}{\pi}\alpha_l\right)^{1/2} Ja$

C_p volumetric specific heat at constant pressure $[J/m^3K]$

$\mathbf{g}$ gravity acceleration vector $[m/s^2]$

h_{fg} latent heat of vaporization $[J/kg]$

Ja Jakob number, equal to $\frac{\rho_l c_{pl}\Delta T}{\rho_g h_{fg}}$

k thermal conductivity $[W/mK]$

$\dot{m}$ volumetric vapor production rate $[kg/m^3s]$

$\mathbf{n}$ interface normal unit vector

p pressure $[Pa]$

$\mathbf{q}$ heat flux vector $[W/m^2]$

R^+ Non-dimensional radius, equal to $\frac{R}{B^2 \,/\, A}$

S_{int} interface surface in a cell $[m^2]$

t^+ Non-dimensional time, equal to $\frac{t}{B^2 \,/\, A^2}$

$\mathbf{u}$ velocity vector $[m/s]$

V_{cell} cell volume $[m^2]$

Greek:

β bubble growth constant

κ interface curvature $[m^{-1}]$

μ dynamic viscosity $[Pa \cdot s]$

ρ density $[kg/m^3]$

σ surface tension coefficient $\left[\frac{N}{m}\right]$

Subscripts:
∞ referring to the bulk fluid
sat referring to saturation conditions

ACKNOWLEDGMENTS

This work has been partially supported by Rolls Royce and EPSRC, and partially supported by a grant from the Swiss National Supercomputing Centre (CSCS) under project ID "psi".

REFERENCES

1. Niceno, B., et al., *Multiscale modelling and analysis of convective boiling: towards the prediction of CHF in rod bundles.* Nuclear Engineering and Technology, 2010. **42**.
2. Podowski, M.Z., *Toward Mechanistic Modeling of Boiling Heat Transfer.* Nuclear Engineering and Technology, 2012. **44**(8): p. 889-896.
3. Bernardin, J.D., et al., *Contact angle temperature dependence for water droplets on practical aluminum surfaces.* International Journal of Heat and Mass Transfer, 1997. **40**(5): p. 1017-1033.
4. Plesset, M.S. and S.A. Zwick, *The growth of vapor bubbles in superheated liquids.* Journal of Applied Physics, 1954. **25**(4).
5. Zwick, S.A. and M.S. Plesset, *On the Dynamics of Small Vapor Bubbles in Liquids.* Journal of Mathematics and Physics, 1955. **33**.
6. Forster, H.K. and N. Zuber, *Growth of a vapor bubble in a superheated liquid.* Journal of Applied Physics, 1954. **25**(4).
7. Forster, H.K. and N. Zuber, *Dynamics of vapor bubbles in boiling heat transfer.* AIChE Journal, 1955. **1**(4).
8. Frenkel, J., *Kinetic theory of liquids*. 1955: Dover.
9. Fisher, J.C., *The fracture of liquids.* Journal of applied physics, 1948. **19**.
10. Lee, H.S. and H. Merte Jr, *Spherical vapor bubble growth in uniformly superheated liquids.* International Journal of Heat and Mass Transfer, 1996. **39**.
11. Scriven, L.E., *On the dynamics of phase growth.* Chemical Engineering Science, 1959. **10**(1-2): p. 1-13.
12. Mikic, B.B., W.M. Rohsenow, and P. Griffith, *On bubble growth rates.* International Journal of Heat and Mass Transfer, 1970. **13**.
13. Han, C.Y. and P. Griffith, *The mechanism of heat transfer in nucleate pool boiling - part 1.* International Journal of Heat and Mass Transfer, 1965. **8**.
14. Lee, H.S. and H. Merte Jr, *Hemispherical vapor bubble growth in microgravity: experiments and model.* International Journal of Heat and Mass Transfer, 1996. **39**.
15. Siegel, R. and C.M. Usiskin, *A photographic study of boiling in the absence of gravity*, 1959, NASA.
16. Usiskin, C.M. and R. Siegel, *An Experimental Study of Boiling in Reduced and Zero Gravity Fields.* Journal of Heat Transfer, 1961. **83**.
17. Merte Jr, H. and J.A. Clark, *Boiling Heat Transfer With Cryogenic Fluidsat Standard, Fractional, and Near-Zero Gravity.* Journal of Heat Transfer, 1964. **86C**.

18. Siegel, R. and E.G. Keshock, *Effects of Reduced Gravity on Nucleate Boiling Bubble Dynamics in Saturated Water.* AIChE Journal, 1964. **10**.
19. Ervin, J.S., et al., *Transient pool boiling in microgravity.* International Journal of Heat and Mass Transfer, 1992. **35**(3).
20. Abe, Y., et al., *Pool boiling of a non-azeotropic binary mixture under microgravity.* International Journal of Heat and Mass Transfer, 1994. **37**(16).
21. Raj, R., J. Kim, and J. McQuillen, *Pool Boiling Heat Transfer on the International Space Station: Experimental Results and Model Verification.* Journal of Heat Transfer, 2012. **134**(10): p. 101504.
22. Warrier, G.R., V.K. Dhir, and D.F. Chao, *Nucleate Pool Boiling eXperiment (NPBX) in microgravity: International Space Station.* International Journal of Heat and Mass Transfer, 2015. **83**: p. 781-798.
23. Brackbill, J.U., D.B. Kothe, and C. Zemach, *A continuum method for modelling surface tension.* Journal of Computational Physics, 1992. **100**.
24. Tryggvason, G., R. Scardovelli, and S. Zaleski, *Direct numerical simulations of gas-liquid multiphase flows*. 2011: Cambridge University Press.
25. Badillo, A., *Quantitative phase-field modeling for boiling phenomena.* Physical Review E, 2012. **86**(4).
26. Alexiades, V. and A.D. Solomon, *Mathematical modelling of melting and freezing processes*. 1993: Hemisphere.
27. Welch, S.W.J. and J. Wilson, *A Volume of Fluid Based Method for Fluid Flows with Phase Change.* Journal of Computational Physics, 2000. **160**(2): p. 662-682.
28. Gibou, F., et al., *A level set based sharp interface method for the multiphase incompressible Navier–Stokes equations with phase change.* Journal of Computational Physics, 2007. **222**(2): p. 536-555.
29. Sato, Y. and B. Ničeno, *A sharp-interface phase change model for a mass-conservative interface tracking method.* Journal of Computational Physics, 2013. **249**: p. 127-161.
30. Versteeg, H. and M. W., *An Introduction to Computational Fluid Dynamics: The Finite Volume Method*. 2007: Prentice-Hall.
31. Sato, Y. and B. Ničeno, *A conservative local interface sharpening scheme for the constrained interpolation profile method.* International Journal for Numerical Methods in Fluids, 2012. **70**(4): p. 441-467.
32. Olsson, E. and G. Kreiss, *A conservative level set method for two phase flow.* Journal of Computational Physics, 2005. **210**(1): p. 225-246.
33. Yokoi, K., *A practical numerical framework for free surface flows based on CLSVOF method, multi-moment methods and density-scaled CSF model: Numerical simulations of droplet splashing.* Journal of Computational Physics, 2013. **232**(1): p. 252-271.
34. Sakashita, H., *Bubble Growth Rates and Nucleation Site Densities in Saturated Pool Boiling of Water at High Pressures.* Journal of Nuclear Science and Technology, 2011. **48**.